Biosensors and Bioelectronics 126 (2019) 187–192

Contents lists available at ScienceDirect

Biosensors and Bioelectronics

journal homepage: www.elsevier.com/locate/bios

A novel electrochemical immunosensor for highly sensitive detection of prostate-specific antigen using 3D open-structured PtCu nanoframes for signal amplification

Yao Chen[a], Pei-Xin Yuan[a], Ai-Jun Wang[a], Xiliang Luo[b], Yadong Xue[c], Lu Zhang[a], Jiu-Ju Feng[a,*]

[a] Key laboratory of the Ministry of Education for Advanced Catalysis Materials, College of Chemistry and Life Sciences, College of Geography and Environmental Sciences, Zhejiang Normal University, Jinhua 321004, China
[b] Key Laboratory of Sensor Analysis of Tumor Marker, Ministry of Education, College of Chemistry and Molecular Engineering, Qingdao University of Science and Technology, Qingdao 266042, China
[c] Jinhua Central Hospital, Jinhua 321001, China

ARTICLE INFO

Keywords:
Prostate-specific antigen
Immunosensor
Hollow nanoframes
Polylysine

ABSTRACT

Herein, a novel electrochemical ultrasensitive immunosensor was designed for detecting prostate-specific antigen (PSA) with three-dimensional (3D) PtCu hollow nanoframes (PtCu HNFs) as signal amplification. The highly opened PtCu HNFs were synthesized by a one-pot solvothermal method with cetyltrimethylammonium chloride (CTAC) and trishydroxymethyl aminomethane (Tris) as co-structuring directors. The architectures enlarged the loading of prostate specific antibodies (Ab) and efficiently catalyzed hydrogen peroxide (H_2O_2) reaction, ultimately amplifying the signals. And polylysine was used to disperse PtCu HNFs, improve the biocompatibility and bind the Ab on the electrode surface. The fabricated immunosensor exhibited lower detection limit (0.003 ng mL^{-1}, $S/N = 3$), and wider linear range (0.01–100.0 ng mL^{-1}), along with the improved reproducibility, selectivity and stability for the assay of PSA. Thus, it is a desirable platform for PSA detection in clinical diagnosis and practical applications.

1. Introduction

Currently, detection of tumor markers has important scientific significance and application prospects for tumor early diagnosis. It's reported that prostate cancer is the most usual malignancy in man and the most common cause of cancer death (Feng et al., 2017). Thus, it is urgent for accurate diagnosis of prostate cancer. In diagnosis and prognosis for early prostate cancer, prostate specific antigen (PSA) is certified as a major biomarker (Yang et al., 2018).

Commonly, enzyme-linked immunosorbent assay (Xuan et al., 2016), chemiluminescence immunoassay (Kim and Lim, 2015), and mass spectrometric immunoassay (Wei et al., 2011) are adopted for diagnosis of prostate cancer. These approaches often require complicated and expensive instruments, and time-consuming operation severely limiting their further use in clinical research and diagnosis, albeit with their high sensitivity and accuracy (Huang et al., 2018). By virtue of highly specific binding between antigens and antibodies (Ab), electrochemical immunosensors have received substantial attention in biomolecular recognition and detection, owing to their enhanced sensitivity, selectivity, simplicity and low-cost (Liu and Ma, 2014; Liu et al., 2017). More importantly, label-free electrochemical immunosensors are very promising due to their facile construction procedures and direct detection (Pan et al., 2017; Wang et al., 2018).

As we all know, advanced nanomaterials play important roles in constructing high-performance electrochemical immunosensors, which are critical to Ab immobilization and signal amplification (Wang et al., 2017). Recently, precious metal nanomaterials have drawn widespread attention in electrochemical immunosensing devices because of their high conductivity, good catalytic activity and stability (Pei et al., 2013; Shi et al., 2018). Among them, Pt-based bimetallic nanomaterials show superior catalytic properties (e.g. high activity, long-term stability and large surface active area), thanks to the synergistic effects between the bimetals alternative to monometallic counterparts (Lu et al., 2017). In particular, three-dimensional (3D) hollow nanoframes (HNFs) have highly open structures and effective molecular available surfaces with abundant active sites, which can load more Ab and accelerate electron transfer process (Nosheen et al., 2013).

Besides, surface modification of nanomaterials can endow them

* Corresponding author.
E-mail address: jjfeng@zjnu.cn (J.-J. Feng).

https://doi.org/10.1016/j.bios.2018.10.057
Received 6 August 2018; Received in revised form 17 October 2018; Accepted 26 October 2018
Available online 29 October 2018
0956-5663/

novel functionality and effectively improve surface properties such as stability, dispersibility and biocompatibility (Song et al., 2014). Biopolymers such as chitosan were widely used for dispersing nanocrystals to construct biosensors (Feng et al., 2005), ultimately improving the stability and biocompatibility and preventing the nanoparticles from aggregating together (Feng et al., 2005; Zhao et al., 2008). Herein, polylysine is a non-toxic, biodegradable, water soluble and stable homo-polypeptide, belonging to the group of cationic biopolymers (Yuan et al., 2018). It widely acts as a drug carrier, achieving effective immobilization of metal ions, enzymes, Ab and other biomolecules (Yuan et al., 2018). Therefore, it is used usually as a dispersant for nanocrystals to construct highly sensitive biosensors (Fakhrullin et al., 2007; Flampouri and Kintzios, 2011; Hua et al., 2012).

Also, trishydroxymethyl aminomethane (Tris, Fig. S1, Supplementary Information, SI) is widely adopted as biological buffer for nucleic acids and proteins (Huisman and Dozy, 1965), which owns an amino group and three hydroxyl groups, displaying certain reducibility under mild conditions and chelating ability (Kim and Lim, 2015). In this work, well-defined 3D PtCu HNFs were synthesized by a Tris-mediated solvothermal method with the aid of cetyltrimethylammonium chloride (CTAC), followed by employing polylysine to further improve the dispersity and biocompatibility (Fig. 1). In the light of the boosted currents for hydrogen peroxide (H_2O_2) reduction catalyzed by PtCu HNFs, a new type of label-free ultrasensitive electrochemical immunosensor was fabricated for detecting PSA.

2. Experimental

2.1. Synthesis of PtCu HNFs

CTAC (160 mg) was added to oleylamine (OAm, 20 mL) under constant stirring at 60 °C to obtain a homogeneous suspension. Then, 16 mg of $Pt(acac)_2$, 7 mg of $CuCl_2{\cdot}H_2O$ and 61 mg of Tris were sequentially put into the above solution, in which the solution color changed from yellow to blue-green. Meanwhile, the mixed solution was ultrasonicated for 30 min, transferred into a Teflon-line stainless autoclave (25 mL), and reacted at 180 °C for 10 h. At last, the PtCu HNFs were collected by centrifugation (5 min, 6000 rpm) and washed completely with the mixture of ethanol and cyclohexane for several times and dried in vacuum at 60 °C.

As control experiments, commercial Pt black and Pt nanoparticles (Pt NPs) were used as contrast catalysts, in which Pt NPs were prepared with individual $Pt(acac)_2$ as the metal precursor while other experimental conditions remained unchanged.

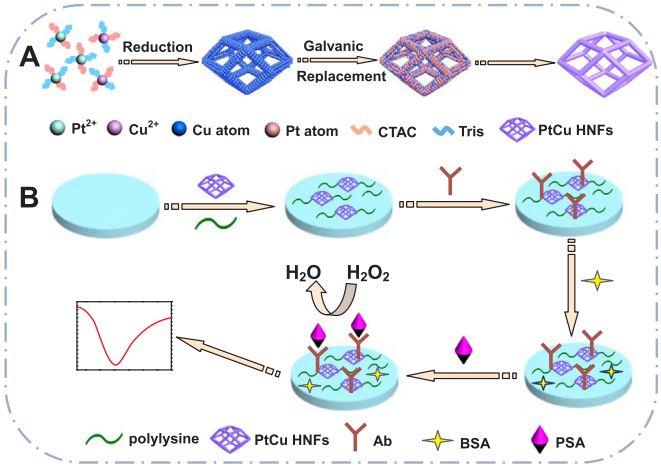

Fig. 1. Schematic diagrams for constructing PtCu HNFs (A) and the correlated electrochemical immunosensor for PSA detection (B).

2.2. Preparation of PtCu HNFs/polylysine

Firstly, 8 mg of polylysine was dissolved into 2 mL of phosphate buffer solution (PBS) (0.1 mol L^{-1}, pH 7.4) under ultrasonication for 40 min to form a well-distributed solution. Next, 1 mL of PtCu HNFs dispersion (4 mg mL^{-1}) were added into the polylysine solution (4 mg mL^{-1}, 1 mL) and then stirred for 5 h. The products were centrifuged at 6000 rpm and washed several times with ethanol and water. Subsequently, the precipitation was re-distributed in PBS for further usage. The stability of PtCu HNFs/polylysine attached on the electrode was evaluated by cyclic voltammetry (CV), as illustrated in Fig. S2 (SI).

2.3. Preparation of PtCu HNFs modified electrode

Fig. 1B describes the scheme for constructing PtCu HNFs-based immunosensor. Firstly, the PtCu HNFs/polylysine dispersion (2 mg mL^{-1}, 6 μL) was dropped onto a freshly-cleaned glass carbon electrode (GCE, 3 mm in diameter), accompanied by drying naturally in air. Next, a prostate specific antibody (Ab) solution (10 μg mL^{-1}, 6 μL) was casted onto the electrode surface and incubated for 1 h, in which PtCu HNFs/polylysine would well immobilize the Ab due to the existence of amino groups in the nanocomposite. After completely washing with PBS, bovine serum albumin (BSA) solution (4 μL, 1 wt%) was put onto the electrode to block nonspecific binding between PSA and the substrate material. Then, the PSA solutions with various concentrations were added onto the electrode surface and incubated for another 30 min. Finally, the immunosensor was totally washed with the above PBS and stored at 4 °C before use. More information of the detailed experiment environment has been provided in SI.

In this study, human serum was received from anonymous donors of Jinhua Central Hospital. The use of human serum for verification of the analytic method is approved by the ethics committee of the hospital and all applicable institutional and governmental regulation concerning the ethical use of human serum were followed.

3. Results and discussion

3.1. Characterization of PtCu HNFs

As shown by the representative transmission electron microscopy (TEM) images at different magnifications (Fig. 2A and B), the sample contains numerous well-defined 3D PtCu HNFs with good dispersion, showing the dodecahedron-like particles. The average particle diameter is roughly 16.91 nm, as described in Fig. S3, SI. The high-resolution TEM (HRTEM) images (Fig. 2a and b) reveal many visible lattice fringes. Furthermore, the lattice spacing distances along the adjacent fringes are calculated to be 0.216 nm and 0.221 nm, which are bounded by the {111} facets of face-centered cubic (*fcc*) PtCu alloy (Lu et al., 2017).

The architectures are further confirmed by high-angle annular dark-field scanning transmission electron microscopy (HAADF-STEM) images (inset in Fig. 2B). Meanwhile, the fast Fourier transforms (FFT) shows the single-crystalline character. And disordered areas emerge from the marked red dotted boxes (Fig. 2B), which are assigned to crystal defects exposing more active sites accessible to enhance the activity of a catalyst (Alloyeau et al., 2009).

The HAADF-STEM and elemental mappings (Fig. 3A-D) display that Pt and Cu atoms homogeneously show up at all nanoframes, verifying the formation of the PtCu alloy (Zhang et al., 2016a). The elemental line scanning profiles (Fig. 3E) further show the uniform distribution of the bimetals, further confirming the formation of the PtCu alloy (Jiang et al., 2017). Importantly, Pt signals are a little stronger than those of Cu throughout the cross section, indicating the slightly higher content of Pt in the alloy. This assumption coincides well with the analysis from the energy dispersive spectroscopy (EDS) pattern (Fig. 3F) where the atomic ratio of Cu to Pt is roughly 48:52, which is well consistent with

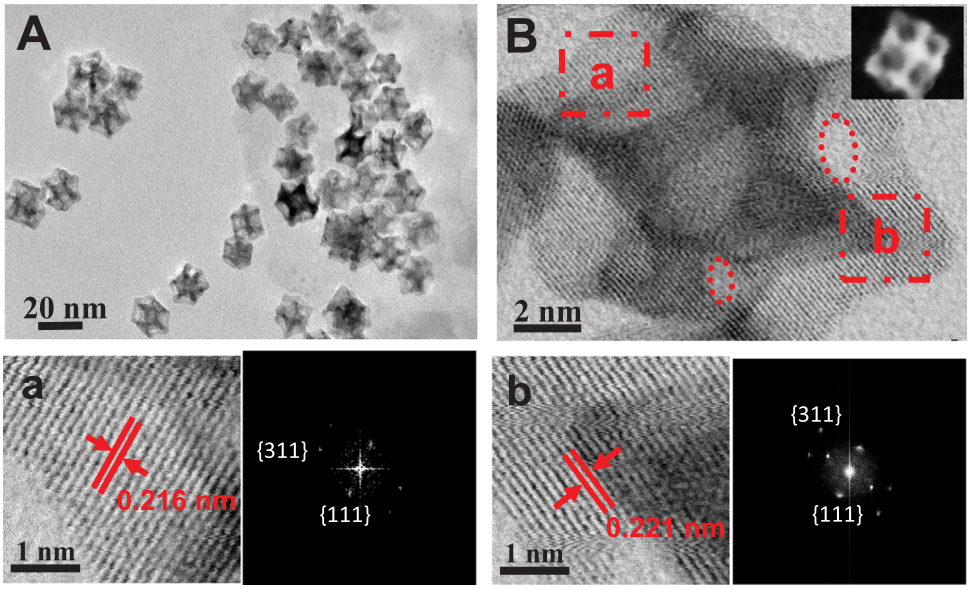

Fig. 2. Medium-magnification TEM images (A) and high-resolution TEM images (B and a–b) of PtCu HNFs. Insets in B shows the HAADF-STEM image. Red dotted boxes indicate the disordered areas. For interpretation of the references to color in this figure legend, the reader is referred to the web version of this article.

the original feeding ratio (1:1) of the two precursors.

X-ray diffraction (XRD) pattern (Fig. S4, SI) shows four peaks located at 42.3°, 49.2°, 72.1° and 87.1°, correlated with the (111), (200), (220) and (311) facets of the *fcc* crystal structure, respectively. It is noted that these peaks appear coincidently between those of Cu (JCPDS-04-0836) and Pt (JCPDS-04-0802), reflecting the PtCu alloyed feature (Jiang et al., 2009). This assumption is further manifested by their upward shifts relative to those of pure Pt (Zhang et al., 2016b) in the binding energy (BE) from the X-ray photoelectron spectra (XPS, Fig. 4A-B), because of the incorporation of Cu atoms (Guo et al., 2017).

As described in Fig. 1A, the formation of PtCu HNFs mainly undergoes two stages: (1) The initial formation of solid dodecahedron-like Cu solid nanoparticles, because Tris, CTA^+ (originated from CTAC), and Cl^- can largely influence the reduction kinetics and crystal behaviors of the two precursors (Zhang et al., 2016b); (2) A galvanic replacement reaction occurs between Cu atoms and the Pt precursor within the confined space at the higher temperature to form alloyed architecture, leading to the ultimate formation of 3D PtCu HNFs (Ding

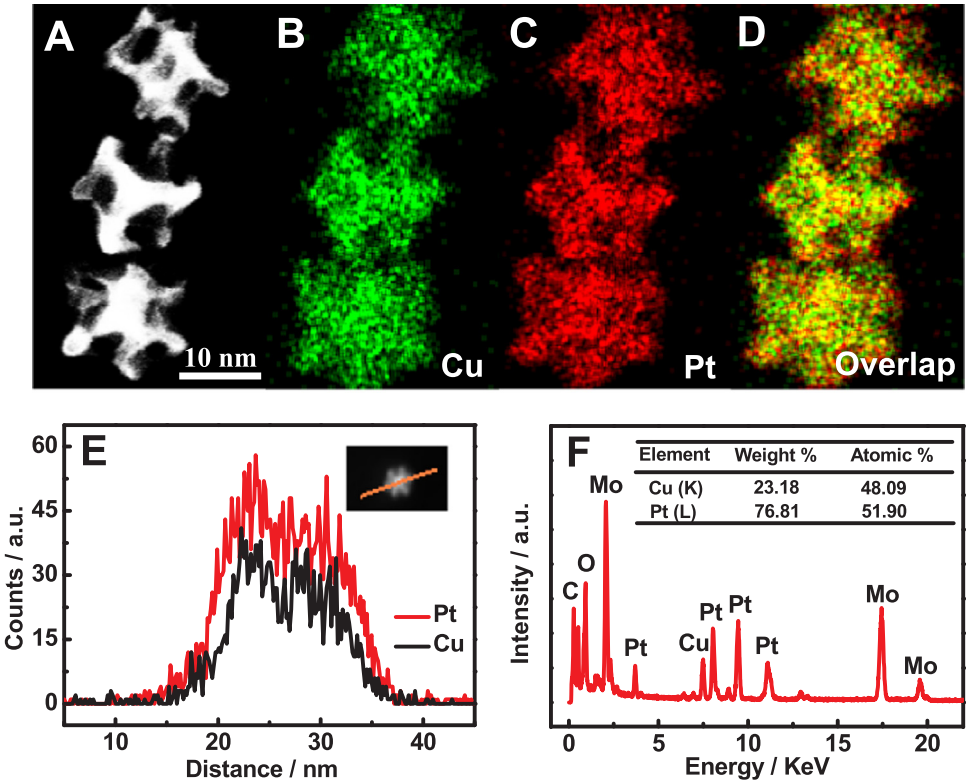

Fig. 3. HAADF-STEM image (A), the elemental mapping images (B-D), line scanning profiles (E), and EDS spectrum (F) of PtCu HNFs. Insets in E and F show the HAADF-STEM image, the weight and atomic ratios of Cu and Pt, respectively.

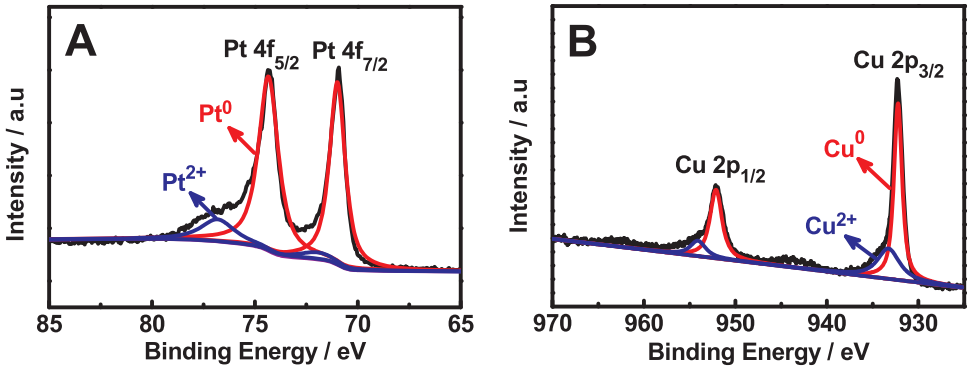

Fig. 4. High-resolution Pt 4f and Cu 2p XPS spectra of PtCu HNFs.

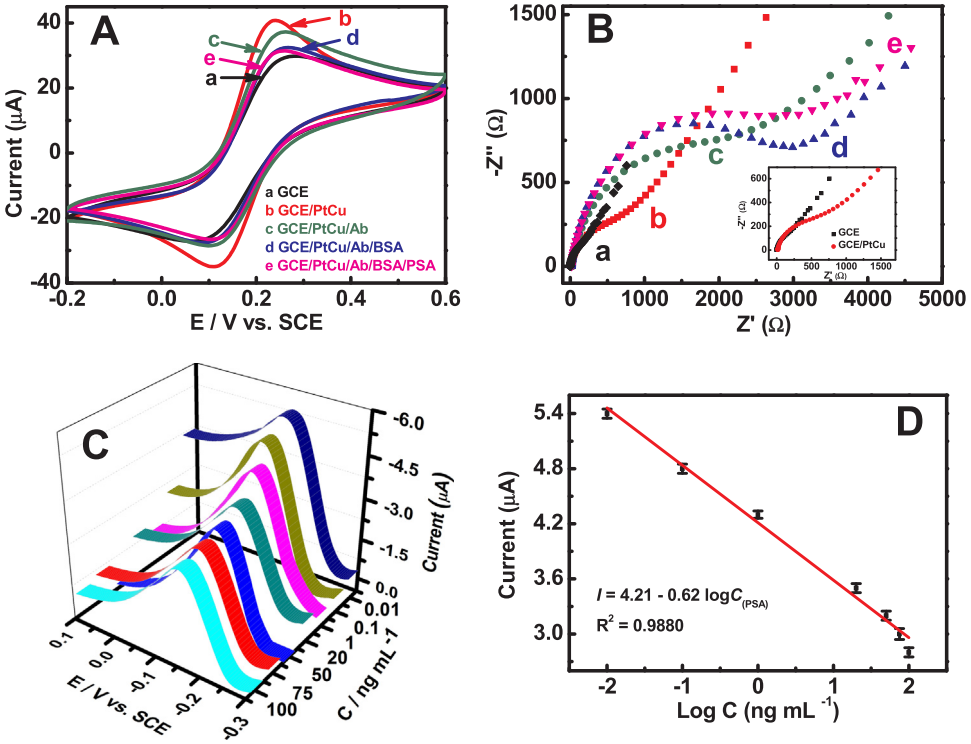

Fig. 5. (A) CV curves and (B) EIS spectra of the fabricated procedures for the immunosensor in 0.1 moL L^{-1} KCl containing 2.5 mmol L^{-1} Fe $(CN)_6^{3-/4-}$. (C) DPV curves of the immunosensor with 0.01, 0.1, 1.0, 20.0, 50.0, 75.0, and 100.0 ng mL^{-1} PSA in 10 mL (0.1 mol L^{-1}, pH 7.4) PBS containing 5.0 mmol L^{-1} H_2O_2. (D) The calibration curves. Error bar = *RSD* (n = 3).

et al., 2015).

In order to compare the catalytic properties of PtCu HNFs with other materials for reducing H_2O_2, the control experiment was conducted by differential pulse voltammetry (DPV), as Fig. S5 (SI) reveals. It is seen that commercial Pt black (curve b) and Pt NPs (curve c) have the greater signals for H_2O_2 reduction. Surprisingly, the responses of PtCu HNFs are further increased due to the synergistic effects between the bimetals and plentiful active sites to improve the catalytic activity. Thus, PtCu HNFs was chosen as an outstanding catalytic material for constructing the immunosensor.

Meanwhile, PtCu HNFs and polylysine were characterized by Fourier transform infrared spectroscopy (FT-IR) and zeta potentials before and after the modification. The characteristic absorption peak of polylysine appears at 1660 cm^{-1} in the respective FT-IR spectrum, which is the stretching vibration of the N-H bond (Fig. S6, SI). However, in the case of PtCu HNFs/polylysine, the absorption peak of polylysine at 1660 cm^{-1} is weakened since the amino groups in polylysine have specific interactions with PtCu HNFs, indicating that polylysine as a dispersant can significantly improve the stability of PtCu HNFs. The PtCu HNFs/polylysine was dispersed in 0.1 mol L^{-1} PBS (pH 7.4). The zeta potential is roughly 0.1583 mV (Table S1, SI), because the dissociation constant of polylysine (pKa = 9.9) is lower as compared with that of blank buffer solution (Purrello et al., 1998).

3.2. Characterization of the fabricated immunosensor

Cyclic voltammetry (CV) is a useful tool for detecting the interface properties of surface-modified electrodes in the fabricated procedure (Li et al., 2017). Fig. 5A shows the CV curves of PtCu HNFs based immunosensors. Obviously, the peak current enhances greatly when compared with that of bare GCE (curve a) after coating with PtCu HNFs/polylysine (curve b). This is ascribed to the greatly enhanced specific area and superior electrical conductivity of PtCu HNFs. However, the peak currents are significantly reduced after the immobilization of anti-PSA (Ab, curve c) and BSA (curve d), due to the fact that the modification is severely inhibited the electron transfer between the probe and the electrode. Furthermore, the peak current is greatly decreased after modifying with PSA (curve e), mainly thanks to the formation of the immune complexes. These observations certify the efficient construction of the immunosensor in this study.

Electrochemical impedance spectroscopy (EIS) is also a powerful technique to monitor the fabricated procedures (Fig. 5B). Obviously, an

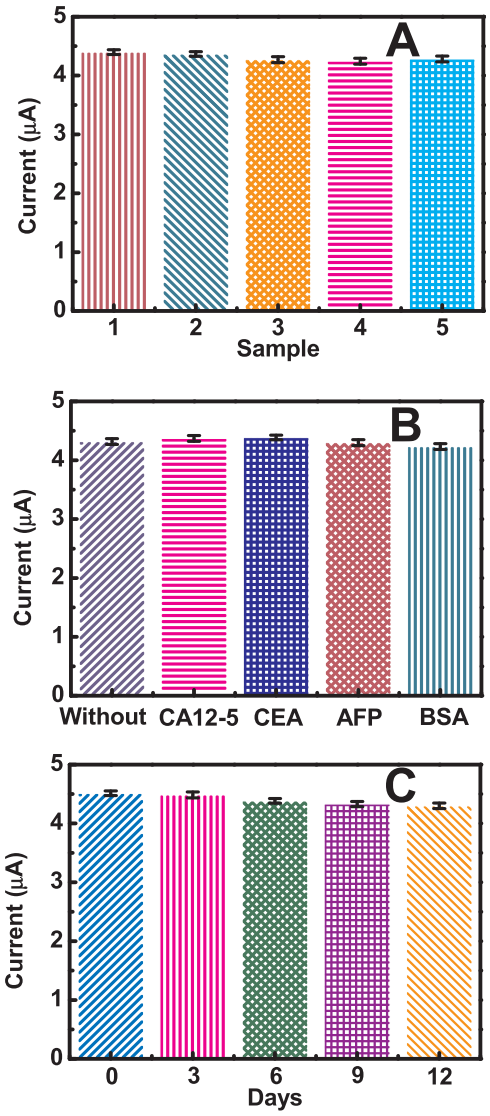

Fig. 6. (A) The peak currents of the five immunosensors fabricated independently in the presence of 1.0 ng mL^{-1} PSA. (B) The currents of the immunosensor towards 1.0 ng mL^{-1} PSA without and with 100.0 ng mL^{-1} CA12-5, CEA, AFP, and BSA. (C) The currents of the immunosensors with different storage time in the presence of 1.0 ng mL^{-1} PSA. Error bar = *RSD* (n = 3).

almost straight line is detected after modification with PtCu HNFs/polylysine (curve b), indicating the electron transfer process of the probe with the electrode is a diffusion-controlled process (Wei et al., 2011). This observation is similar to that of bare GCE (curve a), owing to the superior electric conductivity of PtCu HNFs/polylysine. However, the electron-transfer resistance (R_{et}) values are significantly increased when anti-PSA (curve c) and BSA (curve d) are successively modified on the electrode surface, reflecting their effective immobilization. As expected, the R_{et} is further increased after the modification with PSA (curve e). These results further confirm the effective fabrication of the immunosensor.

3.3. Optimization of immunoassay conditions

The pH of PBS is an important parameter affecting the performance of electrochemical sensors (Weng et al., 2017; Yang et al., 2018). Herein, control experiments regarding the variation in the pH values (5.0–8.0) were first investigated by DPV. As seen in Fig. S7A (SI), the peak currents are largely boosted by enhancing the pH values from 5.0 to 7.4, and then inversely decrease as the pH is higher than 7.4. In the end, the following experiments were performed at pH 7.4.

Meanwhile, the peak currents enhance with the PtCu HNFs concentrations from 0.5 to 2.0 mg mL^{-1}, followed by an adverse trend found by further boosting the concentration up to 2.5 mg mL^{-1} (Fig. S7B, SI). Thus, the PtCu HNFs suspension at 2.0 mg mL^{-1} was the best in this context.

3.4. Analytical performance

DPV was utilized to examine the PSA concentrations on the constructed immunosensor. Fig. 5C shows the catalytic reduction peak currents towards H_2O_2 with the PSA concentrations from 0.01 to 100.0 ng mL^{-1} under the optimal experimental conditions. As shown in Fig. 5D, the currents linearly decrease with the enlarged PSA concentrations with a relatively low detection limit of 0.003 ng mL^{-1} (S/N = 3). Meanwhile, the regression equation is I (μA) = 4.21–0.62 log $C_{(PSA)}$ (ng mL^{-1}) with a correlation coefficient of 0.9880.

To better illustrate the advantages of the as-fabricated immunosensor, Table S2 (SI) displays the comparison with those in the literature. Clearly, the as-constructed immunosensor has a significantly lower detection limit and a broader linear range. Their great enhancement in the analytic performances is principally ascribed to the following three factors: (i) The unique 3D PtCu HNFs with abundant active sites and good electric conductivity would effectively enhance the catalytic activity and accelerate the electron transfer process (He et al., 2016). (ii) The PtCu HNFs can load more Ab due to their unique highly-opened 3D frameworks. (iii) Polylysine displays good biocompatibility and dispersibility, endowing the PtCu alloy with functional groups for efficient binding of antigens and antibodies.

3.5. Reproducibility, selectivity and stability

To test the reproducibility of the immunosensor, five immunosensors were prepared individually for detection of PSA (1.0 ng mL^{-1}) under the same conditions (Fig. 6A). The relative standard deviation (*RSD*) is around 4.31%, revealing desirable accuracy and reproducibility of the immunosensor.

Fig. 6B demonstrates the selectivity of the immunosensor with 1.0 ng mL^{-1} PSA including 100.0 ng mL^{-1} various interferents (e.g. CA-125, CEA, AFP and BSA). The changes of the currents were lower than 4.52% after adding the interferents, indicating the acceptable selectivity of the developed immunosensor for the assay of PSA.

The developed immunosensor was stored at 4 °C when not in use to further investigate it's stability. As illustrated in Fig. 6C, the peak currents were only reduced by 4.70% after 12 days storage, illustrating its long-term durability.

3.6. Analysis of serum sample

To prove the practical applicability of the immunosensor, the recovery was explored by standard addition method. Different concentrations of PSA were added in the human serum sample and then detected. The recovery ranges from 98.3% to 102.3% and the *RSD* is less than 3.66%, as depicted in Table S3 (SI), confirming the promising practicability of the immunosensor for detection of PSA in real serum sample.

To validate the accuracy of the electrochemical immunosensor, the results are compared with commercial ELISA method, as Table S4 (SI) shows. The results of the developed method and ELISA are consistent, confirming the acceptable performances of the prepared immunosensor in clinical testing.

4. Conclusions

To sum up, 3D PtCu HNFs were synthesized by a simple

solvothermal method with CTAC and Tris as the co-structure directors. A new type ultrasensitive electrochemical immunosensor for PSA detection was fabricated by virtue of the boosted H_2O_2 reduction catalyzed by PtCu HNFs. The immunosensor displayed a wider linear range of 0.01–100.0 ng mL^{-1}, with a lower detection limit of 0.003 ng mL^{-1} ($S/N = 3$), a good reproducibility, outstanding selectivity and favorable stability towards PSA detection, indicating its prospective applications in clinical diagnosis.

Acknowledgements

This research was supported by National Natural Science Foundation of China (No. 21475118, 21305124 and 21675093), Basic Public Welfare Research Project of Zhejiang Province (No. GG19BO5003 and LGG18E010001), National Natural Science Foundation of Zhejiang Province (No. Q19B050016), and Foundation of Key Laboratory of Sensor Analysis of Tumor Marker, Ministry of Education, Qingdao University of Science and Technology (No. SATM201703, STAM201804).

Appendix A. Supplementary material

Supplementary data associated with this article can be found in the online version at doi:10.1016/j.bios.2018.10.057.

References

Alloyeau, D., Ricolleau, C., Mottet, C., Oikawa, T., Langlois, C., Le Bouar, Y., Braidy, N., Loiseau, A., 2009. Nat. Mater. 8, 940–946.
Ding, J., Zhu, X., Bu, L., Yao, J., Guo, J., Guo, S., Huang, X., 2015. Chem. Commun. 51, 9722–9725.
Fakhrullin, R.F., Vinter, V.G., Zamaleeva, A.I., Matveeva, M.V., Kourbanov, R.A., Temesgen, B.K., Ishmuchametova, D.G., Abramova, Z.I., Konovalova, O.A., Salakhov, M.K., 2007. Anal. Bioanal. Chem. 388, 367–375.
Feng, J.-J., Zhao, G., Xu, J.-J., Chen, H.-Y., 2005. Anal. Biochem. 342, 280–286.
Feng, J., Li, Y., Li, M., Li, F., Han, J., Dong, Y., Chen, Z., Wang, P., Liu, H., Wei, Q., 2017. Biosens. Bioelectron. 91, 441–448.
Flampouri, E., Kintzios, S., 2011. Procedia Eng. 25, 976–979.
Guo, L., Huang, L.-B., Jiang, W.-J., Wei, Z.-D., Wan, L.-J., Hu, J.-S., 2017. J. Mater. Chem. A 5, 9014–9021.
He, D.-S., He, D.-P., Wang, J., Lin, Y., Yin, P.-Q., Hong, X., Wu, Y., Li, Y.-D., 2016. J. Am. Chem. Soc. 138, 1494–1497.
Hua, L., Wu, X.-Q., Wang, R., 2012. Analyst 137, 5716–5719.
Huang, S., Gan, N., Li, T., Zhou, Y., Cao, Y., Dong, Y., 2018. Talanta 179, 28–36.
Huisman, T.H.J., Dozy, A.M., 1965. J. Chromatogr. A 19, 160–169.
Jiang, K.-Z., Shao, Q., Zhao, D.-D., Bu, L.-Z., Guo, J., Huang, X.-Q., 2017. Adv. Funct. Mater. 27, 1700830.
Jiang, S., Ma, Y., Jian, G., Tao, H., Wang, X., Fan, Y., Lu, Y., Hu, Z., Chen, Y., 2009. Adv. Mater. 21, 4953–4956.
Kim, S., Lim, H.B., 2015. Talanta 140, 183–188.
Li, M., Wang, P., Li, F., Chu, Q., Li, Y., Dong, Y., 2017. Biosens. Bioelectron. 87, 752–759.
Liu, N., Ma, Z.-F., 2014. Biosens. Bioelectron. 51, 184–190.
Liu, Y., Weng, X., Wang, K.-K., Xue, Y., Wang, A.-J., Wu, L., Feng, J.-J., 2017. Sens. Actuators B: Chem. 247, 349–356.
Lu, B.-G., Sheng, T., Tian, N., Zhang, Z.-C., Xiao, C., Cao, Z.-M., Ma, H.-B., Zhou, Z.-Y., Sun, S.-G., 2017. Nano Energy 33, 65–71.
Nosheen, F., Zhang, Z.-C., Zhuang, J., Wang, X., 2013. Nanoscale 5, 3660–3663.
Pan, M., Gu, Y., Yun, Y., Li, M., Jin, X., Wang, S., 2017. Sensors 17, 1041–1164.
Pei, X., Zhang, B., Tang, J., Liu, B., Lai, W., Tang, D., 2013. Anal. Chim. Acta 758, 1–18.
Purrello, R., Bellacchio, E., Gurrieri, S., Lauceri, R., Raudino, A., Scolaro, L.M., Santoro, A.M., 1998. J. Phys. Chem. B 102, 8852–8857.
Shi, Y.-C., Wang, A.-J., Yuan, P.-X., Zhang, L., Luo, X., Feng, J.-J., 2018. Biosens. Bioelectron. 111, 47–51.
Song, J.-B., Duan, B., Wang, C.-X., Zhou, J.-J., Pu, L., Fang, Z., Wang, P., Lim, T.T., Duan, H.-W., 2014. J. Am. Chem. Soc. 136, 6838–6841.
Wang, R., Feng, J.-J., Liu, W.-D., Jiang, L.-Y., Wang, A.-J., 2017. Biosens. Bioelectron. 96, 152–158.
Wang, R., Liu, W.-D., Wang, A.-J., Xue, Y.-D., Wu, L., Feng, J.-J., 2018. Biosens. Bioelectron. 99, 458–463.
Wei, Q., Zhao, Y.-F., Du, B., Wu, D., Cai, Y.-Y., Mao, K.-X., Li, H., Xu, C.-X., 2011. Adv. Funct. Mater. 21, 4193–4198.
Weng, X., Liu, Y., Xue, Y., Wang, A.-J., Wu, L., Feng, J.-J., 2017. Sens. Actuators B: Chem. 250, 61–68.
Xuan, Z., Li, M., Rong, P., Wang, W., Li, Y., Liu, D., 2016. Nanoscale 8, 17271–17277.
Yang, Y.-Y., Yan, Q., Liu, Q., Li, Y.-P., Liu, H., Wang, P., Chen, L., Zhang, D.-P., Li, Y.-Y., Dong, Y.-H., 2018. Biosens. Bioelectron. 99, 450–457.
Yuan, J., Guo, L., Wang, S.-J., Liu, D., Qin, X., Zheng, L.-L., Tian, C.-L., Han, X.-H., Chen, R., Yin, R.-H., 2018. Colloids Surf. B 171, 406–412.
Zhang, N., Bu, L.-Z., Guo, S.-J., Guo, J., Huang, X.-Q., 2016a. Nano Lett. 16, 5037–5043.
Zhang, Z., Luo, Z., Chen, B., Wei, C., Zhao, J., Chen, J., Zhang, X., Lai, Z., Fan, Z., Tan, C., Zhao, M., Lu, Q., Li, B., Zong, Y., Yan, C., Wang, G., Xu, Z.-J., Zhang, H., 2016b. Adv. Mater. 28, 8712–8717.
Zhao, X.-J., Mai, Z.-B., Kang, X.-H., Zou, X.-Y., 2008. Biosens. Bioelectron. 23, 1032–1038.